PCCP

Cite this: *Phys. Chem. Chem. Phys.*, 2012, **14**, 2983–2990

www.rsc.org/pccp

PAPER

In situ time-resolved DXAFS study of Rh nanoparticle formation mechanism in ethylene glycol at elevated temperature†

Hiroyuki Asakura,[a] Kentaro Teramura,[a] Tetsuya Shishido,[a] Tsunehiro Tanaka,*[a] Ning Yan,[b] Chaoxian Xiao,[c] Siyu Yao[c] and Yuan Kou*[c]

Received 28th September 2011, Accepted 5th December 2011
DOI: 10.1039/c2cp23070d

A combination of *in situ* time-resolved DXAFS and ICP-MS techniques reveals that the formation process of Rh nanoparticles (NPs) from rhodium trichloride trihydrate ($RhCl_3{\cdot}3H_2O$) in ethylene glycol with polyvinylpyrrolidone (PVP) at elevated temperature is a first-order reaction, which indicates that uniform size Rh NPs appear consecutively and these Rh NPs do not aggregate with each other.

Introduction

Metal nanoparticles (NPs) are getting much more attention than ever in both fields of fundamental science and engineering. Metal NPs have several unique properties or applications, such as surface plasmon resonance,[1] magnetism,[2,3] imaging,[4] or catalysis.[5] For example, metal NPs have several catalytic activities, such as hydrogenation by Rh NPs,[6–8] and C–C coupling reaction by Pd NPs.[9,10]

These days, various scientists' efforts have enabled us to control NP size and/or shape. Their formation mechanisms are also vigorously investigated, but still under discussion. To the best of our knowledge, there are two common formation mechanisms of NPs proposed by LaMer[11] and Finke.[12,13] LaMer *et al.* studied the formation mechanism of sulphur sol to propose that the sol is formed by simultaneous nucleation from a supersaturated solution of monomer and its growth is by attachment of monomers to the resulting nuclei. On the other hand, Finke *et al.* have studied the formation kinetics and mechanism of iridium NPs from iridium precursors by H_2 reduction. They proposed a different mechanism from LaMer in that the nuclei are formed slowly but constantly and the NPs grow mainly by autocatalytic reduction of metal precursors on the particle surface, which can be called a two step mechanism[12] or a four step mechanism for transition metal NP formation and agglomeration.[13] The Finke–Watzky two step mechanism of Ir nanoparticle preparation with hydrogen can be summarized with the equation below.

$$[A]_t = (k_a/k_b + [A]_0)/(1 + (k_a/k_b[A]_0)\exp(k_a + k_b[A]_0)t) \quad (1)$$

where k_a and k_b are the average rate constants for nucleation and autocatalytic growth, respectively. $[A]_t$ and $[A]_0$ are the concentrations of nanocluster precursor A at reaction time of t and 0, respectively.[12] X-ray absorption near-edge structure (XANES) and extended X-ray absorption fine structure (EXAFS) spectroscopy was regarded as a potentially powerful method for directly observing the nucleation process of nanoparticles.[14] Indeed, several research groups have recently applied X-ray absorption fine structure (XAFS) measurements to investigate the formation mechanism of NPs. For example, Harada *et al.* has investigated Pt,[15] Rh,[16,17] Pd,[17] Ag,[18] and Au[19] metal NP formation by photoreduction in polymer solutions and confirmed the two step mechanism proposed by Finke *et al.* Nishimura *et al.* studied the formation mechanism of Cu NPs in aqueous PVP solution with $NaBH_4$ reduction at ambient conditions by means of *in situ* quick XAFS technique (QXAFS) in fluorescence mode and found that stable intermediates such as $Cu(OH)_2$ and Cu^+-PVP were formed during an induction period of nucleation of Cu NPs.[20] Our research group have investigated the photodeposition process of Rh cations on a TiO_2 photocatalyst by means of *in situ* dispersive XAFS (DXAFS) technique and proposed consecutive deposition of Rh NPs,[21,22] and the nucleation and growth process of Au nanoparticles by means of the newly developed *in situ* fast QXAFS technique and found a four atom Au cluster during the induction period.[23,24]

In this study, we applied *in situ* time-resolved XAFS technique in order to understand the formation mechanism of Rh NPs in ethylene glycol (EG) at elevated temperature.[25–28]

[a] *Kyotodaigaku-katsura, Nishikyo, Kyoto, Japan. E-mail: tanakat@moleng.kyoto-u.ac.jp; Fax: +81 75 383 2561; Tel: +81 75 383 2562*
[b] *Institut des Sciences et Ingenierie Chimiques, Ecole Polytechnique Federale de Lausanne (EPFL), CH-1015, Lausanne, Switzerland. E-mail: yan.ning@epfl.ch; Fax: +41 21 693 98 85; Tel: +41 21 693 98 54*
[c] *PKU Green Chemistry Centre, Beijing National Laboratory for Molecular Sciences, College of Chemistry and Molecular Engineering, Peking University, Beijing, 100871, China. E-mail: yuankou@pku.edu.cn; Fax: +86 10 62751708; Tel: +86 10 62757792*
† Electronic supplementary information (ESI) available. See DOI: 10.1039/c2cp23070d

Interestingly, the Rh NP growth does not seem to occur during NP formation and Finke's two-step mechanism in the case of photoreduction condition could satisfactorily address all the experimental observations and a distinct scenario could be envisaged for Rh NP formation in EG at elevated temperatures.

Experimental

Materials and general procedures of Rh NP preparation

$RhCl_3{\cdot}3H_2O$ (Wako, Japan), polyvinylpyrrolidone (PVP) (M_w = 40 000, Yili Chemical, China), and ethylene glycol (EG) (Wako, Japan) were purchased and used without further purification. Rh NPs were prepared as follows. $RhCl_3{\cdot}3H_2O$ and PVP are dissolved into appropriate amount of EG with sonication and are poured into a tube reactor equipped with Dimroth condenser. The concentration of Rh is 0.02 mol L^{-1} and the Rh/PVP ratios are 1/15, 1/30 or 2/15 (Rh: 0.04 mol L^{-1}). Reaction conditions are summarized in Table 1.

In situ Rh K-edge dispersive XAFS measurement and data reduction

In situ time-resolved Rh K-edge XAFS spectra were recorded at the BL28B2 beamline of the SPring-8 (Ako, Japan). The DXAFS measurement system consists of a polychromator set to a Laue configuration with a Si(422) net plane and a position-sensitive detector (PSD) mounted on a θ–2θ diffractometer (Scheme 1). The size of an X-ray focal spot on the sample is 0.16 mm in width and 2.4 mm in length and the distance between the polychromator and the sample, and the sample and PSD are 920 mm and 640 mm, respectively. The total energy bandwidth is 22 950–24 010 eV. The X-ray energy was calibrated by the spectrum of a Rh foil. The oil bath filled with silicon oil was placed on a movable stage. A side-arm Pyrex reactor equipped with Dimroth condenser and thermocouple was fixed with a clamp and immersed into the reaction solution at around the X-ray focal spot. In the beginning of the DXAFS measurement, the oil bath was automatically moved up to heat the tube reactor, thus there are some delays between the starting time of DXAFS measurements and that of solution heating. The exposure time of the PSD depends on the contents of the reaction mixture because the X-ray transparency of each reaction mixture is different. Usually, one hundred shots were accumulated for spectral quality. Data reduction of the XAFS spectra was performed through a previously described[22] procedure by REX2000[29] (Rigaku, Japan). The k^3-weighted EXAFS oscillation in the range of 2.8–11 $Å^{-1}$ was Fourier transformed. Linear combination fitting (LCF) of a series of XANES spectra was performed with Athena included in IFEFFIT package.[30] In the LCF procedure, the absorption edges (E_0) of the reference spectra were fixed and the sum of the weights of the reference spectra was also fixed to 1 and each weight was between 0 and 1. Fitting was performed in a range of photon energies between −30 eV to 50 eV from E_0 as base position in all cases.

Table 1 Summary of experimental conditions

Run	[Rh]/mol L^{-1}	[PVP]/mol L^{-1}	Temperature[a]/°C
A	0.02	0.30	135
B	0.02	0.30	100
C	0.02	0.60	125
D	0.04	0.30	125

[a] Temperature was measured by a thermocouple immersed into the reaction mixture.

ICP-MS

The EG solution containing both Rh NPs and Rh^{3+} were first treated with ultrafiltration in special tubes (Amicon Ultra 0.5 ml Ultracel 3 k) over a centrifuge operating at 12 000 rpm for 0.5 h. The filtrate was diluted, digested by 10% HNO_3 and finally was diluted again to match an acid concentration of about 1%.

An Agilent 7500ce ICP-MS, interfaced to a CETAC CEI-100 microconcentric nebulizer, was used to determine the Rh content in the aqueous phase. Instrument control as well as data analysis was carried out using ChemStation B.03.03 software. The nebulizer was operated in self-aspiration mode with the sheath liquid (50 mM formic acid, 20 ppb Ge) closing the electrical circuit. Analyses were only started when a sufficiently stable signal (RSD 72Ge < 5%) was obtained. An ICP-MS tuning solution containing lithium, yttrium, cerium, thallium, and cobalt in 2% HNO_3 (each 10 mg L^{-1}, Agilent Technologies) was used for calibration.

TEM observation

The high resolution transmission electronic microscope (HR-TEM) images were taken with a Tecnai F20 microscopy operating under 200 kV accelerating voltage and JEOL JEM-2100F operating at an accelerating voltage of 200 kV. The samples were prepared as follows. Rh nanoparticles were precipitated from the EG solution after addition of 4 quantities of acetone (*v*/*v*), then separated by centrifugation (10 000 rpm for 5 min). Finally, the precipitate was re-dispersed in an appropriate amount of methanol (0.08 mol L^{-1}) under ultrasonication. One drop of the above solution containing Rh nanoparticles was deposited on carbon-coated copper grids and dried at room temperature *in vacuo*.

Results and discussion

TEM observation

Fig. 1 shows TEM images of Rh NP samples obtained during the Rh NP formation reaction of 0.02 mol L^{-1} $RhCl_3{\cdot}3H_2O$ and PVP/EG solution (Rh/PVP = 1/15) at 403 K after reaction for 5, 10, 30, and 120 min. All Rh NPs were observed as multipod-type NPs and their average width of branch is

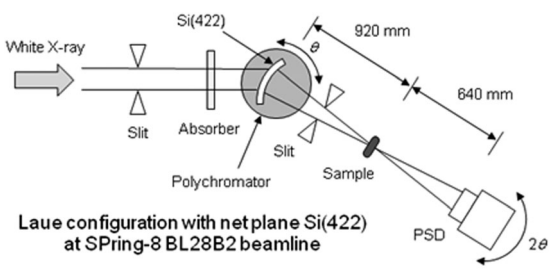

Scheme 1 Main equipment of the DXAFS spectroscopy system at the BL28B2 beamline.

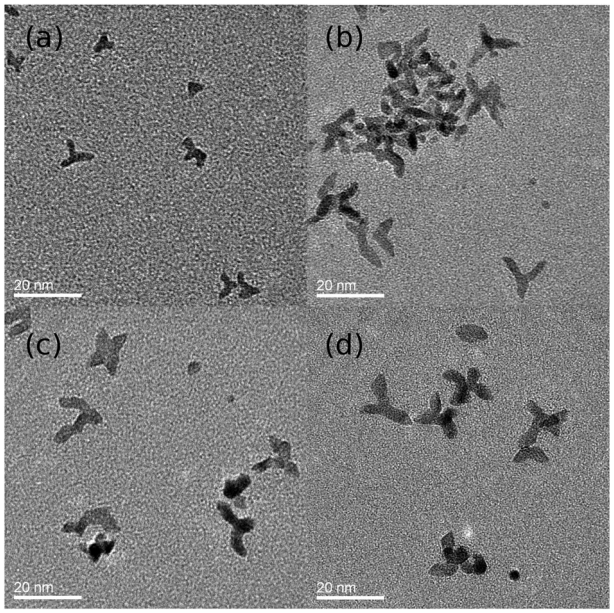

Fig. 1 TEM images of Rh NPs under conditions of $RhCl_3{\cdot}3H_2O$ = 0.02 mol L^{-1}, Rh/PVP = 1/15, 403 K after reaction for (a) 5 min, (b) 10 min, (c) 30 min, (d) 120 min.

ca. 3 nm and the average length of the particles is *ca.* 12 nm. However, at the very beginning, the elongation of the branch is observed in Fig. 1(a) and (b). It may be because of the aggregation of the small Rh units to the multipod NPs, but there is no evidence in the present study.

Fig. 2 shows TEM images of Rh NP samples obtained during the Rh NP formation reaction of a 0.02 mol L^{-1} $RhCl_3{\cdot}3H_2O$ and PVP/EG solution (Rh/PVP = 1/15) at 373 K (*e.g.* run B) after the reaction for 25, 35, 65, and 85 min. All Rh NPs were observed as multipod-type NPs and

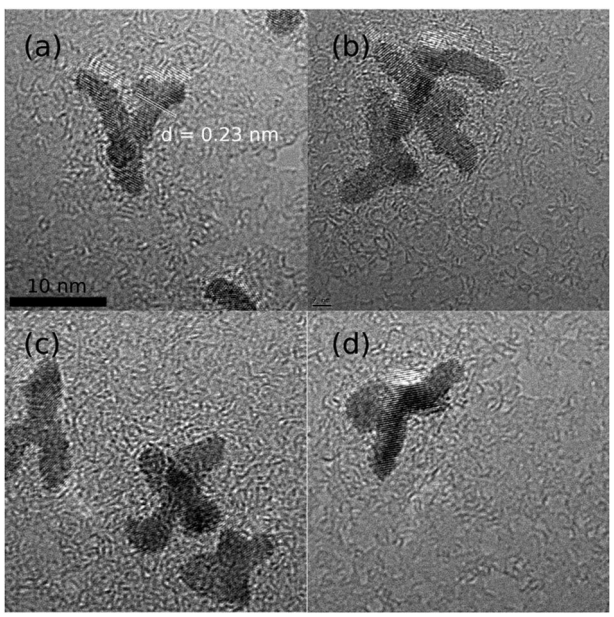

Fig. 2 TEM images of Rh NPs under conditions of $RhCl_3{\cdot}3H_2O$ = 0.02 mol L^{-1}, Rh/PVP = 1/15, 373 K after reaction for (a) 25 min, (b) 35 min, (c) 65 min, (d) 85 min.

their average particle size is as same as run A. These results indicate that the Rh NP size did not grow under these reaction conditions once formed.

Rh K-edge *in situ* dispersive XAFS measurement

$RhCl_3{\cdot}3H_2O$ with PVP in EG. Fig. 3 shows a series of Rh K-edge XANES spectra of the reaction mixture of $RhCl_3{\cdot}3H_2O$ and PVP EG solution (Rh/PVP = 1/15) (run A) and the reference spectra of $RhCl_3{\cdot}3H_2O$ (solid) and Rh foil. The exposure time of the X-ray on the reaction mixture is 66 ms and a good quality XAFS spectra was obtained with accumulation every 6.6 s to form a series of spectra. The XANES spectrum of the initial state is similar to that of the $RhCl_3{\cdot}3H_2O$. The shift of X-ray absorption edge energy (E_0) from 23 229 eV to 23 224 eV indicates a reduction of Rh^{3+} cation to Rh^0 species during the polyol process. The XANES spectra after 15 min thermal reduction were similar to that of the Rh foil as presented in Fig. 3(a). The XANES spectra gradually changed from that of the Rh^{3+} cation to that of the Rh^0 metal with an isosbestic point at around 23 259 eV. Thus, the Rh^{3+} ions are reduced to Rh^0 during the polyol process without any intermediates on the second timescale.

All Rh K-edge XANES spectra were reproduced with the linear combination fitting of XANES spectra of the initial state (Rh^{3+}; before heating) and Rh foil. Fig. 4 shows the time course of the fractions of initial state of Rh^{3+} precursor and Rh foil, respectively. The exponential decay of the fraction of Rh^{3+} indicated that the Rh NP formation process depends with pseudo-first order kinetics on Rh^{3+} concentration. It is noteworthy that the final XANES spectrum is seen to consist

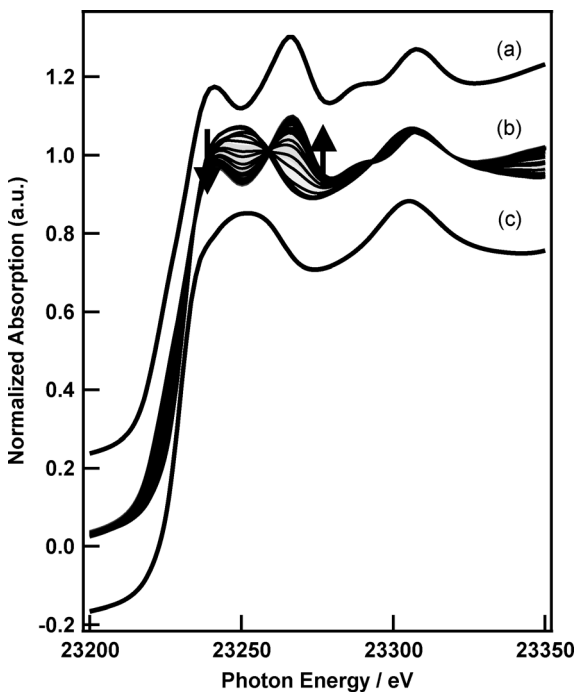

Fig. 3 Rh K-edge XANES spectra (a) Rh foil, (b) a series of Rh K-edge XANES spectra of reaction solution containing $RhCl_3{\cdot}3H_2O$ at 408 K for 1 h, and PVP in EG (run A), (c) $RhCl_3{\cdot}3H_2O$. (Arrows indicate spectral change for 1 h).

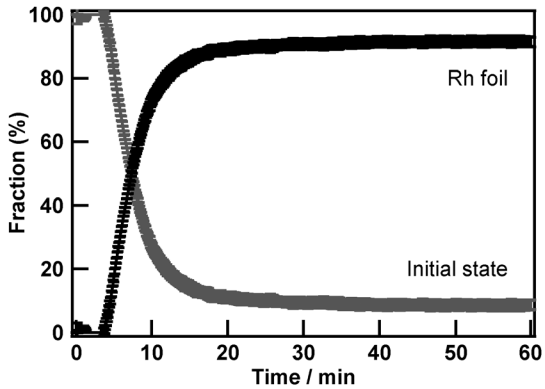

Fig. 4 Time course of two fractions of a series of XANES spectra during the polyol process at 408 K for 1 h (run A). XANES spectra of initial state (gray cross) and Rh foil (black circle) were used for standard spectra of linear combination fitting.

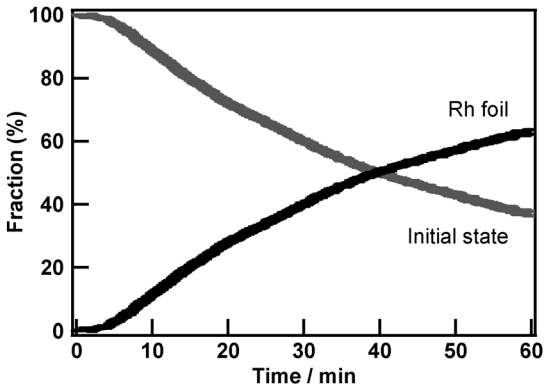

Fig. 6 Time course of two fractions of a series of XANES spectra during the polyol process at 373 K for 1 h (run B). XANES spectra of initial state (gray cross) and Rh metal (black circle) were used for the standard spectra of linear combination fitting.

of *ca.* 90% of Rh foil and *ca.* 10% Rh^{3+} because the XANES spectrum of NPs is usually different from that of bulk state.[23]

Fig. 5 shows a series of Rh K-edge XANES spectra of the reaction mixture during the Rh NPs preparation from $RhCl_3{\cdot}3H_2O$ with PVP in EG (Rh/PVP = 1/15) at 373 K for 1 h (run B). In this case, the XANES spectra also gradually changed from that of the Rh^{3+} cation to that of the Rh^0 metal with the isosbestic point at around 23 259 eV, but the final XANES spectrum is not identical to that of Rh foil because the reduction of Rh^{3+} did not complete.

To determine the progress rate of Rh NP formation, these spectra were analyzed by linear combination fitting of initial state and Rh metal again (Fig. 6). The Rh^{3+} consumption rate looks like pseudo-first order kinetics just as at 408 K, but the Finke–Watzky mechanism is also possible. Thus, we attempted to fit the decay of the initial state fraction with eqn (1) and simple exponential curve based on the pseudo-first order kinetics (supporting information†). As shown in Fig. S4 and S5,† the fitting precision with exponential curve is higher than that with eqn (1) since eqn (1) is based on the assumption that the rate of the nucleation and the autocatalytic growth is similar to each other. The stable trend of the first few minutes is not well matched with the model of eqn (1) because the temperature rapidly increased (see Fig. S7†). In the present system, the autocatalytic step is much faster than the nucleation step. Thus, the pseudo-first order kinetics is a much better hypothesis for the present reaction.

Fig. 7 shows the time course of the value of $\ln([Rh^{3+}(t)]/[Rh^{3+}(0)])$ against reaction time, which exhibits a clear linear relationship and the slope is 0.0179 min^{-1}. We also evaluated the Rh^{3+} consumption rate by means of ultrafiltration and ICP-MS technique under the same condition.

Fig. 8 shows the time course of the value of $\ln([Rh^{3+}(t)]/[Rh^{3+}(0)])$ evaluated by ICP-MS. The value of $\ln([Rh^{3+}(t)]/[Rh^{3+}(0)])$ clearly depends on reaction time in a linear manner and the slope is 0.0169 min^{-1}, which is an observed kinetic constant. Thus, the Rh^{3+} consumption rate is consistent with the *in situ* DXAFS results and obeys (pseudo) first order kinetics. As mentioned above, the essence of the Finke–Watzky mechanism[12] is that the precursor is consumed by two elementary steps, which are the direct reduction of precursor over reductant and catalytic reduction of precursor over the surface atoms on NPs, and in the same process, new metal–metal bond forms. Under these scenarios, the rate law of Rh^{3+} is expressed as

$$r = k_{obs}[Rh^{3+}]^x = k_1[Rh^{3+}] + k_2[Rh^{3+}][Rh^0] \qquad (2)$$

After derivation, it can be found that the apparent reaction order "x" could not be 1 (which is the fitting results of

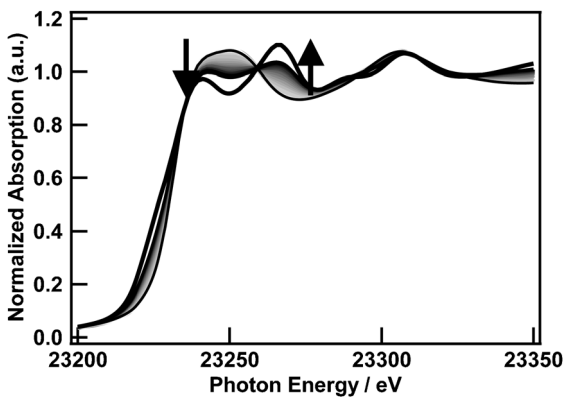

Fig. 5 A series of Rh K-edge XANES spectra of a reaction solution containing $RhCl_3{\cdot}3H_2O$, and PVP in EG at 373 K for 1 h (run B; arrows indicate spectral change for 1 h) (thick black line: Rh foil).

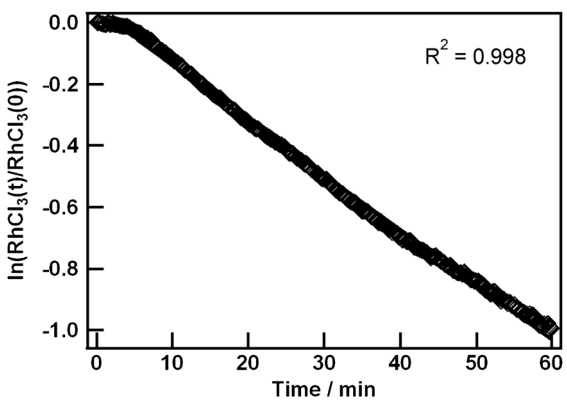

Fig. 7 Time course of $\ln([Rh^{3+}(t)]/[Rh^{3+}(0)])$ derived from linear combination fitting of XANES (run B).

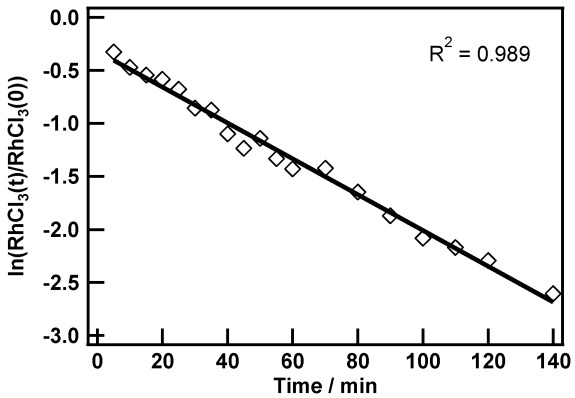

Fig. 8 Time course of $\ln([Rh^{3+}(t)]/[Rh^{3+}(0)])$ derived from $[Rh^{3+}(t)]$ evaluated by ultrafiltration and ICP-MS.

the DXAFS and ICP-MS data) unless $[Rh^0]$ = constant (which is clearly against reality) or $k_1 \gg k_2[Rh^0]$ (which means the second step is neglectable). Therefore, the dominant pathway of Rh^{3+} reduction in our system appears to be the direct reaction between Rh^{3+} and ethylene glycol. Next, we carried out *in situ* DXAFS experiments in the condition of Rh/PVP = 1/30 (run C), 2/15 (run D) at 398 K to investigate the effect of the Rh^{3+} or PVP concentration. In run C or D, the overall change of XAFS spectra during Rh NP formation is similar to that of run A (see supporting information†).

First, we calculate the apparent kinetic constant k_{obs} of run A in the same manner as Fig. 7 and it was found to be 0.0219 min^{-1}. From the Arrhenius plot of the kinetic constants of run A and run B, the kinetic constant at 398 K was estimated to be 0.0112 min^{-1} and the activation energy of the reduction step of Rh^{3+} is estimated to be 90.6 kJ mol^{-1}.

The results of linear combination analysis of the XANES spectra of run C and D are shown in Fig. 9. In Run C, the concentration of PVP is fourfold denser than that in run D. However, the fraction changes are almost identical to each other. This indicates PVP concentration has no effect on the Rh NP formation process and may only affect the final size of

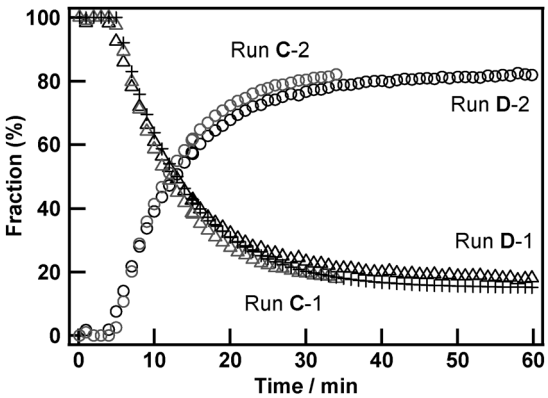

Fig. 9 Change of two fractions of a series of XANES spectra during polyol process at 393 K for 1 h (Rh/PVP = 1/30 (run C), Rh/PVP = 2/15 (run D)). XANES spectra of initial state ("1", triangle) and Rh foil ("2", circle) were used for standard spectra of linear combination fitting. Cross plots are used to calculate Rh^{3+} consumption at 398 K.

Rh NPs. Cross plots are used to calculate Rh^{3+} consumption at 398 K ("run E") using the kinetic constant above and on the assumption that the final XANES spectrum is similar to those in run C and D. The Rh^{3+} consumption rates in run C, D and the calculated "run E" are also identical to each other. This result is consistent with the fact that the Rh NPs formation rate depends on the concentration of Rh^{3+} in first order kinetics as discussed above.

Fig. 10 shows a series of Rh K-edge EXAFS oscillations (run B) and reference spectra of $RhCl_3{\cdot}3H_2O$ and Rh foil. The EXAFS oscillation of Rh foil is divided in half for clarity. It is clearly observed that the $RhCl_3{\cdot}3H_2O$ contribution to the obtained EXAFS oscillation gradually decreased and the Rh metal contribution increased through a single isosbestic point, just as in their XANES spectra.

Fig. 11 shows a series of Fourier transformed Rh K-edge EXAFS spectra (run B), which are not phase corrected and hence the atomic distance (x axis) does not indicate the actual bond length. The peak located at 1.80 Å is assignable to the convolution of Rh–Cl scattering of $RhCl_3$ and Rh–O scattering of Rh ions coordinated to the oxygen of EG. The height of the peak at 1.80 Å decreased as reaction time advances, and an alternative peak appeared at 2.42 Å, which is assigned to the Rh–Rh scattering of Rh NPs generated during the polyol process, in comparison to the Fourier transformed EXAFS spectrum of the Rh foil as a reference. The peak height at 2.42 Å rose during the reaction, but the growth of the peak is not saturated because the reduction of Rh precursor was not completed, as shown in Fig. 5 and 6.

To evaluate the structural parameters of the Rh precursor at the initial state and the Rh NPs at the saturated final state, curve fitting analyses on the initial and final EXAFS spectra of run A and their results are summarized in Table 2.

For the initial spectrum, the coordination numbers of the Rh–Cl and Rh–O shells are estimated to be 3.4 and 1.9, respectively. These parameters indicate that the structure of the initial Rh precursor can be express as $RhCl_3(EG^2)$ or $RhCl_3(PVP)(EG^1)$ where EG^2 means the coordination of two oxygens of two hydroxyl groups of ethylene glycol, EG^1 means the coordination of one oxygen of two hydroxyl groups of

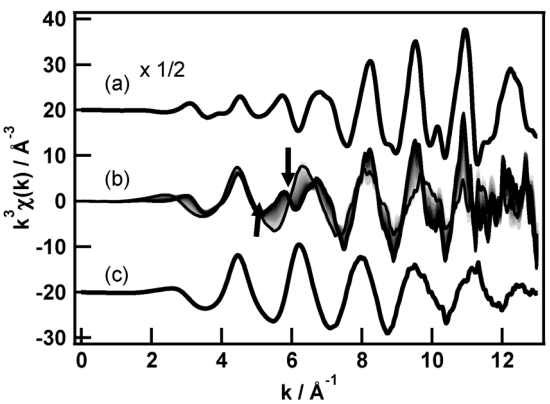

Fig. 10 Rh K-edge EXAFS spectra (a) Rh foil (×1/2), (b) a series of Rh K-edge EXAFS spectra of reaction solution containing $RhCl_3{\cdot}3H_2O$ at 373 K for 1 h, and PVP in EG (run B), (c) $RhCl_3{\cdot}3H_2O$. (Arrows indicate spectral change for 1 h).

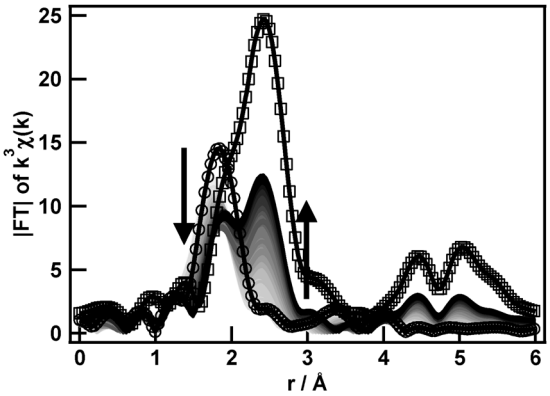

Fig. 11 A series of Fourier transformed spectra of k^3-weighted Rh K-edge EXAFS of reaction solution containing $RhCl_3{\cdot}3H_2O$ at 373 K for 1 h, and PVP in EG (run B; circle: $RhCl_3{\cdot}3H_2O$; square: Rh foil) (phase correction has not been performed).

Table 2 Structural parameters obtained from the curve fitting analysis of the initial and final EXAFS spectra (Rh/PVP = 1/15, 408 K, 1 h, run A)[a]

Ab–Sc[b]	CN[c]	r^d/Å	DW/Å^{-2} [e]	R^f
Initial	—	—	—	—
Rh–Cl	3.4	2.31	0.0031	0.00221
Rh–O	1.9	2.06	0.0028	—
Final	—	—	—	—
Rh–Rh	10.2	2.68	0.0047	0.00126

[a] For the initial spectrum: Δk = 2.8–11 Å^{-1}, ΔR = 0.9–2.3 Å; the curve fitting procedure is performed by REX2000 with backscattering factor and phase shift parameters obtained from $RhCl_3{\cdot}3H_2O$ and Rh_2O_3 standard samples. Other conditions are the same as the final spectrum described below. For final spectrum: Δk = 2.8–11 Å^{-1}, ΔR = 1.7–2.9 Å; the curve fitting procedure is performed by Artemis with back scattering and phase shift parameters calculated by FEFF ver. 8.40, and fell within the Nyquist criteria. Curve fitting was done in R space. R factor is defined as $R = \sum_{i}^{N_{pts}} \frac{[\mathrm{Im}(\chi_{dat}(R_i)-\chi_{th}(R_i))]^2+[\mathrm{Re}(\chi_{dat}(R_i)-\chi_{th}(R_i))]^2}{[\mathrm{Im}(\chi_{dat}(R_i))]^2+[\mathrm{Re}(\chi_{dat}(R_i))]^2}$ where i = 1, 2,…, N_{pts}, N_{pts}: number of data points, χ_{dat}: EXAFS oscillation of experimental data, χ_{th}: EXAFS oscillation of theoretical data. [b] X-ray absorbing and scattering atoms. [c] Coordination number. [d] Atomic distance. [e] XAFS Debye–Waller factor. [f] R factor.

ethylene glycol and PVP means the coordination of one oxygen of pyrrolidone moiety. However, in general, an EXAFS spectrum reflects an averaged coordination environment of Rh species. Moreover, it is known that an aqueous solution of rhodium chloride consists of several Rh species which can be expressed as $Rh(H_2O)_nCl_{(6-n)}$ (n = 1, 2, …, 6) by means of a ^{103}Rh NMR study.[31] Thus, the structure of the initial Rh species is still unknown. However, for the final spectrum, the Rh–Rh atomic distance of the Rh NPs is 2.68 Å, which is slightly shorter than 2.70 Å of the Rh foil model structure input into the FEFF program for parameter calculation, indicating the smallness of the obtained Rh NPs. The coordination number, 10.2, also indicates small Rh NPs. If the shape of the Rh NPs is spherical, CN 10.2 is assignable to a particle size of *ca.* 3.0 nm.

It is difficult to associate the obtained EXAFS spectra directly with the obtained Rh NPs because the shape of the Rh NPs is of a multipod-type. From the HRTEM image of typical Rh NPs (Fig. 12), the multipod-type NPs can be imagined to be aggregated material of spherical NPs (average particle size: *ca.* 3 nm). We believe that curve fitting results of the EXAFS spectra are consistent with the obtained Rh NP shape.

In order to verify our hypothesis that uniform size Rh NPs are generated consecutively, we utilized the EXAFS spectra. EXAFS spectra obtained in transmission mode reflects the averaged state of the target element. In this case, each EXAFS spectrum is a combination of Rh^{3+} and Rh metallic species. The aforementioned ICP-MS study revealed the time course of the concentration of Rh^{3+} species. Thus, the EXAFS spectrum originated from Rh NPs can be calculated by subtracting the Rh^{3+} contribution from each EXAFS spectrum. As shown in Fig. 7, the reduction of Rh^{3+} started at 2 min ($=t_0$) and its reaction constant k_{obs} was obtained as 0.0169 min^{-1}. Thus, the Rh^{3+} ratio of the reaction mixture is expressed as

$$(Rh^{3+}\ \text{ratio}) = \exp(-k_{obs}(t - t_0))\ (t \geqq t_0) \qquad (3)$$

where t is reaction time, and the absorption of XAFS spectrum at time t was calculated by subtracting the Rh^{3+} contribution from each original EXAFS spectrum and normalized by the Rh^0 species concentration, which is expressed as

$$\mu t(t; Rh^0) = (\mu t(t) - (Rh^{3+}\ \text{ratio}) \times \mu t(t = t_0))/(1 - (Rh^{3+}\ \text{ratio})) \qquad (4)$$

where $\mu t(t)$ is the absorption of XAFS spectrum at time t, $\mu t(t; Rh^0)$ is the calculated absorption of XAFS spectrum of Rh^0 species at time t.

Fig. 13 shows a series of Fourier transformed calculated Rh K-edge EXAFS spectra ($\mu t(t; Rh^0)$). The first several spectra are not shown because almost all of them are derived from the Rh^{3+} species and have a lot of noise. The peak height at 2.42 Å is almost constant during the reaction, which indicates that the shape and size of the Rh^0 species in the reaction mixture do not change during reaction, at least from 12 min to 60 min.[32,33] The XANES region of the calculated XAFS spectrum shows an identical spectrum to each other from 12 min onwards (supporting information†). This result also indicates that the once formed Rh NPs did not grow anymore. Finally, to have some insight of the nucleation step, we focused attention on the intensity change of the Fourier transformed EXAFS spectra at 2.42 Å.

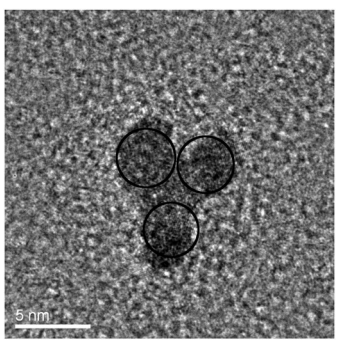

Fig. 12 HRTEM image of Rh NPs under conditions of $RhCl_3{\cdot}3H_2O$ = 0.02 mol L^{-1}, Rh/PVP = 1/15, 403 K after reaction for 120 min.

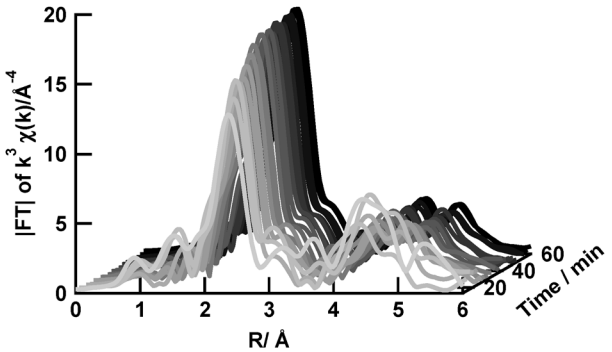

Fig. 13 A series of calculated and Fourier transformed spectra of k^3-weighted Rh K-edge EXAFS from run B.

Fig. 14 shows some plots of the intensity of Fourier transformed EXAFS spectra. The first several plots are not shown because of the same reason above. These FT of EXAFS spectra are almost identical to each other, and it indicates again the continuous generation of uniform Rh NPs. Moreover, when we performed curve fitting analyses on the series of Rh K-edge EXAFS spectra (Fig. 11), the coordination number change of the Rh–Rh shell resulted in a constant value (*ca.* 9.7), which is comparable to the curve fitting analysis of the final EXAFS spectrum of run A.

To shed light on the nucleation step in this condition, we paid attention to the initial change of FT of EXAFS. Fig. 15 shows the temporal change of intensities of Fourier transformed EXAFS spectra at 1.80 Å and 2.42 Å (run B). Over the first 5 min of the NP formation, the peak intensity at 1.80 Å gradually decreased (dissociation of the ligand), but that at 2.42 Å did not change at all. This phenomenon might be interpreted to be an observation of a small amount of $(Rh^0)_n$ (n = 1, 2, 3…) nuclei formation. Namely, at this first step, a portion of Rh^{3+} precursor was reduced by EG to form the $(Rh^0)_n$ nuclei and the chloride anion or oxygen of EG dissociated from $(Rh^0)_n$ because of a lowering ionic bond strength. However, the concentration of $(Rh^0)_n$ species is very dilute, so the explicit Rh–Rh bond is not observed in the FT of EXAFS at this step.

This study is summarized as follows. Using a combination of *in situ* time-resolved DXAFS, ICP-MS, and TEM observation, the following scheme for the Rh NPs formation mechanism is

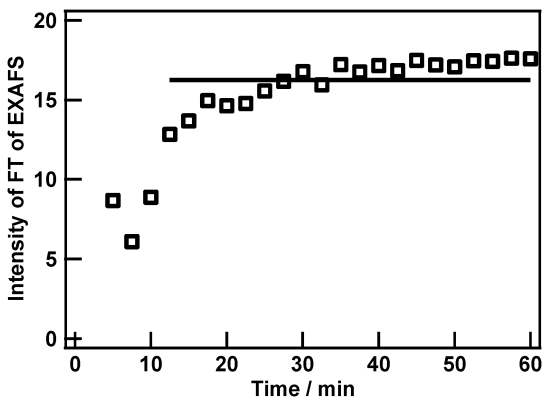

Fig. 14 Intensity of Fourier transformed EXAFS spectra at 2.42 Å (Rh–Rh) as a function of time (plotted the values from the peak intensity at 2.42 Å of Fig. 13).

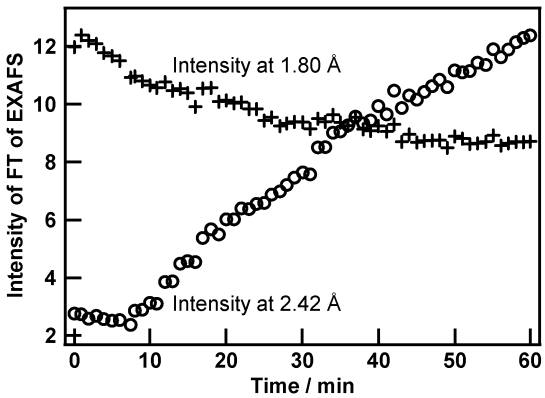

Fig. 15 The temporal change of intensity of Fourier transformed EXAFS spectra (run B).

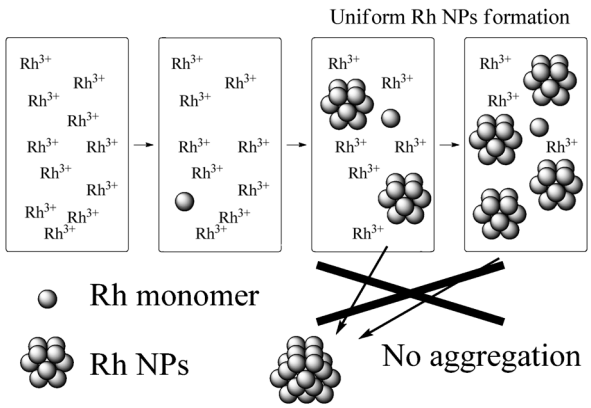

Scheme 2 Schematic view of Rh NP formation mechanism in the present condition.

suggested (Scheme 2). In the first step of Rh NPs formation, Rh^{3+} precursor might be thermally reduced by EG to nucleate to be Rh^0 monomer. In the second step, the Rh NPs formed very rapidly to be uniform size NPs, which are stable under the reaction conditions. The last step is a repeat of the second step, which is the repeat of uniform Rh NP formation.

Conclusions

The polyol process of Rh NP formation, which was performed in the presence of $RhCl_3$ as a precursor, PVP as a capping reagent and ethylene glycol as medium, was observed by *in situ* time-resolved DXAFS measurement, TEM and ICP-MS analysis. These analyses revealed that the polyol process of Rh species proceeds with pseudo-first order kinetics of Rh precursor concentration, and produces Rh NPs of a uniform size. PVP concentration does not affect the Rh NP formation, at least under the present conditions.

Acknowledgements

This work was partially supported by a Grant-in-Aid for Scientific Research (B) (No.22360338) from the Japan Ministry of Education, Culture, Sports, Science and Technology (MEXT). The XAFS measurements at the SPring-8 were carried out with the approval of Japan Synchrotron Radiation

Research Institute (JASRI) (Proposal No. 2010B1676 and 2011A1584). H. A. thanks Grant-in-Aid for Japan Society for the Promotion of Science (JSPS) Fellows and financial support from JASRI for XAFS experiments. N. Y. thanks the Marie Curie Incoming Fellowship (Number: 252125-TCPBRCBDP) for financial support.

Notes and references

1 K. L. Kelly, E. Coronado, L. L. Zhao and G. C. Schatz, *J. Phys. Chem. B*, 2003, **107**, 668–677.
2 T. Hyeon, *Chem. Commun.*, 2003, 927–934.
3 A. Lu, E. L. Salabas and F. Schüth, *Angew. Chem., Int. Ed.*, 2007, **46**, 1222–1244.
4 I. L. Medintz, H. T. Uyeda, E. R. Goldman and H. Mattoussi, *Nat. Mater.*, 2005, **4**, 435–446.
5 N. Yan, C. Xiao and Y. Kou, *Coord. Chem. Rev.*, 2010, **254**, 1179–1218.
6 N. Yan, Y. Yuan and P. J. Dyson, *Chem. Commun.*, 2011, **47**, 2529–2531.
7 R. R. Dykeman, N. Yan, R. Scopelliti and P. J. Dyson, *Inorg. Chem.*, 2011, **50**, 717–719.
8 X. Yang, N. Yan, Z. Fei, R. M. Crespo-Quesada, G. Laurenczy, L. Kiwi-Minsker, Y. Kou, Y. Li and P. J. Dyson, *Inorg. Chem.*, 2008, **47**, 7444–7446.
9 Y. Li, X. M. Hong, D. M. Collard and M. A. El-Sayed, *Org. Lett.*, 2000, **2**, 2385–2388.
10 Y. Li and M. A. El-Sayed, *J. Phys. Chem. B*, 2001, **105**, 8938–8943.
11 V. K. LaMer and R. H. Dinegar, *J. Am. Chem. Soc.*, 1950, **72**, 4847–4854.
12 M. A. Watzky and R. G. Finke, *J. Am. Chem. Soc.*, 1997, **119**, 10382–10400.
13 C. Besson, E. E. Finney and R. G. Finke, *J. Am. Chem. Soc.*, 2005, **127**, 8179–8184.
14 E. E. Finney and R. G. Finke, *J. Colloid Interface Sci.*, 2008, **317**, 351–374.
15 M. Harada and H. Einaga, *Langmuir*, 2006, **22**, 2371–2377.
16 M. Harada, D. Abe and Y. Kimura, *J. Colloid Interface Sci.*, 2005, **292**, 113–121.
17 M. Harada and Y. Inada, *Langmuir*, 2009, **25**, 6049–6061.
18 M. Harada, Y. Inada and M. Nomura, *J. Colloid Interface Sci.*, 2009, **337**, 427–438.
19 M. Harada and H. Einaga, *Langmuir*, 2007, **23**, 6536–6543.
20 S. Nishimura, A. Takagaki, S. Maenosono and K. Ebitani, *Langmuir*, 2010, **26**, 4473–4479.
21 K. Teramura, S. Okuoka, S. Yamazoe, K. Kato, T. Shishido and T. Tanaka, *J. Phys. Chem. C*, 2008, **112**, 8495–8498.
22 J. Ohyama, K. Teramura, S. Okuoka, S. Yamazoe, K. Kato, T. Shishido and T. Tanaka, *Langmuir*, 2010, **26**, 13907–13912.
23 J. Ohyama, K. Teramura, Y. Higuchi, T. Shishido, Y. Hitomi, K. Kato, H. Tanida, T. Uruga and T. Tanaka, *ChemPhysChem*, 2011, **12**, 127–131.
24 J. Ohyama, K. Teramura, Y. Higuchi, T. Shishido, Y. Hitomi, K. Aoki, T. Funabiki, M. Kodera, K. Kato, H. Tanida, T. Uruga and T. Tanaka, *Phys. Chem. Chem. Phys.*, 2011, **13**, 11128–11135.
25 J. D. Hoefelmeyer, K. Niesz, G. A. Somorjai and T. D. Tilley, *Nano Lett.*, 2005, **5**, 435–438.
26 Y. Borodko, S. M. Humphrey, T. D. Tilley, H. Frei and G. A. Somorjai, *J. Phys. Chem. C*, 2007, **111**, 6288–6295.
27 S. M. Humphrey, M. E. Grass, S. E. Habas, K. Niesz, G. A. Somorjai and T. D. Tilley, *Nano Lett.*, 2007, **7**, 785–790.
28 Y. Zhang, M. E. Grass, J. N. Kuhn, F. Tao, S. E. Habas, W. Huang, P. Yang and G. A. Somorjai, *J. Am. Chem. Soc.*, 2008, **130**, 5868–5869.
29 T. Taguchi, T. Ozawa and H. Yashiro, *Phys. Scr.*, 2005, **T115**, 205–206.
30 B. Ravel and M. Newville, *J. Synchrotron Radiat.*, 2005, **12**, 537–541.
31 C. Carr, J. Glaser and M. Sandström, *Inorg. Chim. Acta*, 1987, **131**, 153–156.
32 A. Jentys, *Phys. Chem. Chem. Phys.*, 1999, **1**, 4059–4063.
33 R. E. Benfield, *J. Chem. Soc., Faraday Trans.*, 1992, **88**, 1107–1110.

